Full-scale experimental assessment of a radiant-capacitive cooling system driven by nocturnal and diurnal radiative cooling

Original
Full-scale experimental assessment of a radiant-capacitive cooling system driven by nocturnal and diurnal radiative cooling / González-Cruz, E., Pérez, G., Frutos, B., Alonso, C., Martin-Consuegra, F., Gutierrez, Á., Krüger, E., Pattelli, L.. - In: BUILDING AND ENVIRONMENT. - ISSN 0360-1323. - 304:(2026). [10.1016/j.buildenv.2026.115136]

Availability:
This version is available at: 11696/90200 since: 2026-08-24T22:46:04Z

Publisher:
Elsevier

Published
DOI:10.1016/j.buildenv.2026.115136

Building and Environment 304 (2026) 115136

Contents lists available at ScienceDirect

Building and Environment

journal homepage: www.elsevier.com/locate/buildenv

Full-scale experimental assessment of a radiant-capacitive cooling system driven by nocturnal and diurnal radiative cooling

Eduardo González-Cruz [a], Gloria Pérez [a,*], Borja Frutos [a], Carmen Alonso [a], Fernando Martin-Consuegra [a], Álvaro Gutierrez [b], Eduardo Krüger [c], Lorenzo Pattelli [d]

[a] Instituto de Ciencias de la Construcción Eduardo Torroja (IETCC), CSIC, Madrid, Spain
[b] Universidad Politécnica de Madrid (UPM), Madrid, Spain
[c] Universidade Tecnológica Federal do Paraná – UTFPR, Curitiba, Brasil
[d] Istituto Nazionale di Ricerca Metrologica (INRIM), Torino, Italy

ARTICLE INFO

Keywords:
Nighttime radiative cooling
Daytime radiative cooling
Full-scale experiment
Thermal performance
Radiant-capacitive cooling system
Passive cooling
Hydronic system

ABSTRACT

We demonstrate a full-scale radiant-capacitive cooling system (RCCS) capable of maintaining continuous thermal comfort during hot summer conditions without using mechanical refrigeration, thanks to a combination of sky radiators with water-filled radiant-capacity ceiling panels. Tested in twin full-scale cells under clear-sky conditions, the RCCS maintained operative temperatures within the adaptive comfort limit for 94% of the monitoring period when uncoated and for 100% when the radiators were coated with a commercial passive daytime radiative cooling (PDRC) material. The experimental cell exhibited temperatures on average 6–7 K cooler than the control cell, with peak daily reductions in indoor maximum temperature up to 12 K. Sky radiators produced a median cooling potential of about 56 W m^{-2} (43–74 W m^{-2} across the series), while the ceiling panels removed an average of 2.8–3.2 kWh per day (432–494 Wh/m^{2}•day), depending on configuration. Applying the PDRC material extended effective cooling by 2–4 h per day and increased daily delivered cooling energy by more than 10%. Multiple-regression models based on climatic and operational variables explain the observed temperature reductions and cooling potential of the sky radiators. These results indicate that a low-complexity, water-based radiative cooling system built from widely available components can significantly improve thermal comfort in well-insulated buildings during extreme heat without mechanical refrigeration.

1. Introduction

The global rise in greenhouse gas emissions, largely driven by energy use in buildings, is a critical environmental challenge. Space cooling currently accounts for around 20% of building electricity demand and about 10% of global energy use [1]. With cooling demand expected to increase tenfold by 2050 [2] and heatwaves intensifying due to global warming and urbanization [3], there is an urgent need for cooling strategies that reduce energy use and dissipate heat with minimal environmental impact. In this context, the principle of “cooling without heating” should guide the development of sustainable solutions for the built environment.

Passive radiative cooling (PRC) has re-emerged as a promising strategy by using outer space as a vast heat sink, taking advantage of the low atmospheric emittance in the 8–13 μm wavelength range, particularly under dry conditions [4]. Historically, nocturnal radiative cooling has been used in buildings in applications such as ice production [5], and many systems have been proposed to harness energy-free cooling via the atmospheric infrared window, mainly at night [6–11]. The introduction of selective-surface radiators in the 1970s further improved performance under clear skies by tailoring their spectral properties to maximize long-wave emission [12].

Passive radiative cooling systems use the sky dome as a heat sink but are constrained by low radiative energy and nighttime conditions. Recent advances include geometric optimization, such as a vertical-fin radiative sky-cooling method that combines multi-directional cooling with improved convective heat transfer via vertical profiles [13]. Scaling these approaches to buildings requires thermodynamic models and feasibility analyses of deep-space-source heat pumps to determine boundary conditions and seasonal performance [14]. Advances in nanotechnology and thermal photonics have produced PRC materials that strongly reflect solar radiation while emitting in the mid-infrared,

* Corresponding author.
E-mail address: gperezaq@ietcc.csic.es (G. Pérez).

https://doi.org/10.1016/j.buildenv.2026.115136
Received 17 April 2026; Received in revised form 11 August 2026; Accepted 15 August 2026
Available online 16 August 2026

achieving sub-ambient temperatures under direct sunlight [15]. Since then, substantial research has focused on PRC materials, radiative cooling panels, and the design and optimization of ceiling panels for radiant cooling in buildings. Several reviews summarize the state of the art in passive daytime radiative cooling (PDRC) technologies and materials [16–20]. Passive daytime radiative cooling technology is being integrated into several high-impact sectors, including building envelopes, where its application in rooftop and facade coatings can reduce air-conditioning energy use by more than 60% [21]. However, despite promising laboratory results and theoretical developments, significant gaps remain regarding the real-world applicability and robustness of PRC-based systems in full-scale buildings, where multiple environmental and operational variables interact. The long-term durability, optical performance, and energy-saving potential of passive daytime radiative cooling (PDRC) coatings are critical factors in determining their practical viability. Although PDRC can cool buildings without energy consumption, its real-world application depends on the ability of these coatings to preserve their optical properties after years of outdoor exposure [22].

Complementary full-scale experiments in different climates [23–25], including some with radiative cooling systems [26], have provided valuable data for validating numerical models, which are essential for sensitivity analyses, system optimization and performance assessment in practice.

In this context, the present research demonstrates a full-scale, water-based radiant-capacitive cooling system (RCCS) deployed in twin test cells under hot summer conditions, reconciling component-level geometry with systemic macro-feasibility without mechanical refrigeration. The system integrates high-capacity modular ceiling panels with day-and-night radiative sky radiators coated with PDRC materials, as well as thermal energy storage. This setup builds upon previous dual radiant-capacitive heating and cooling configurations tested in Curitiba, Brazil (Köppen–Geiger Cfb climate) [11,27], that lacked daytime PDRC materials. The current study is conducted at the full-scale experimental facility of the Eduardo Torroja Institute for Construction Science in Arganda del Rey, Madrid, Spain [28], characterized by a Csa–Bsk climate with hot, dry summers and limited rainfall—conditions that are particularly suitable for assessing PRC-based cooling strategies [29,30].

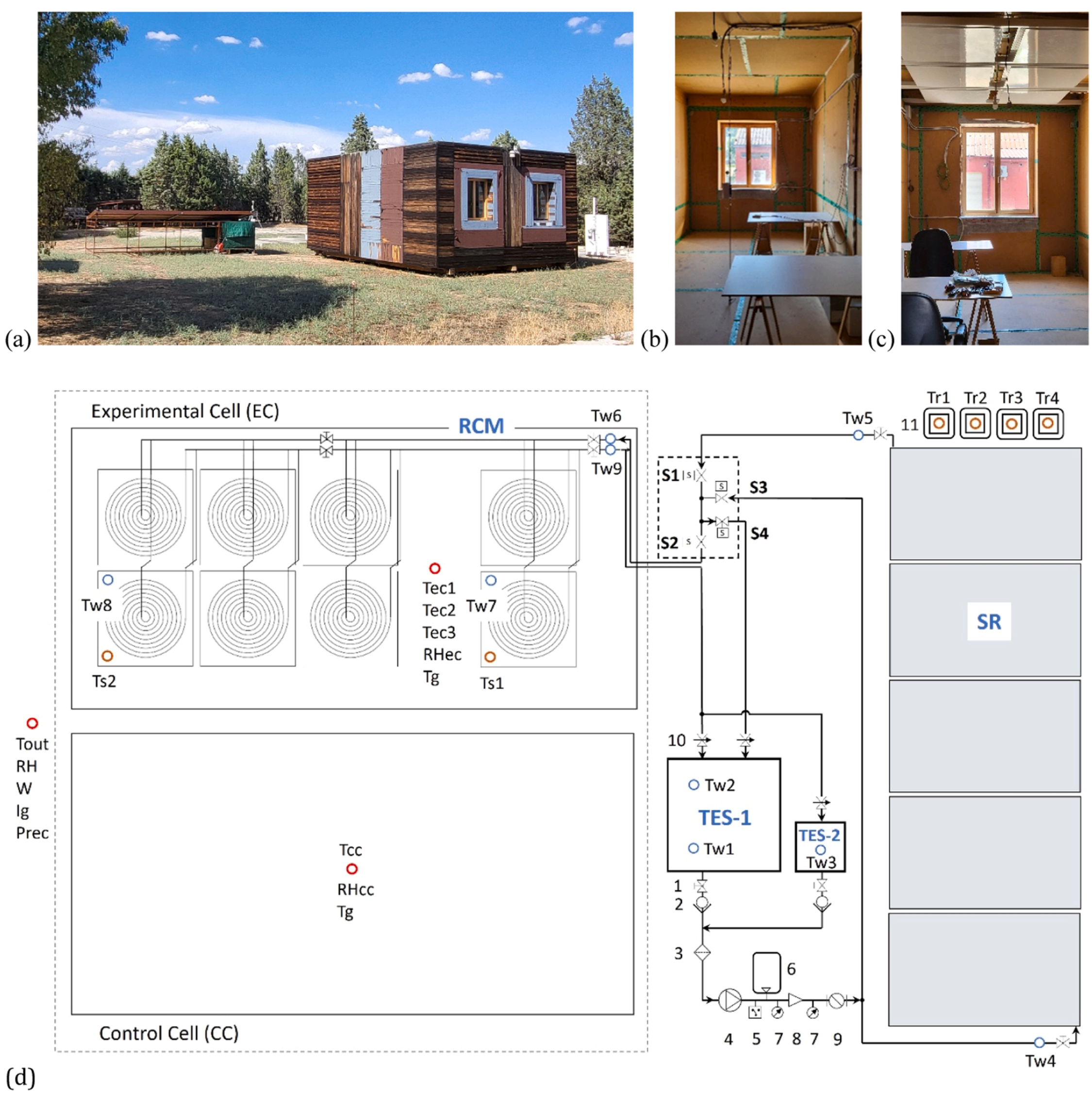

Fig. 1. (a) The full-scale experimental facility with two test cells (Experimental and Control) featuring south-facing windows. (b) Interior view of the control cell. (c) Interior view of the experimental cell. (d) Component diagram of the radiant-capacitive cooling system. The system includes: RCM (8 radiant-capacitive modules); SRs (5 sky radiators); TES (2 thermal energy storage); S1, S2, S3 and S4 (solenoid valves); 1: Gate valve; 2: Check valve; 3: Water filter; 4: Water pump; 5: Pressure switch; 6: Pressure tank; 7: Pressure gauge; 8: Pressure control valve; 9: Water flow meter; 10: Needle valve; and 11: Reference sample materials. The measurement location of variables detailed in Table 3 are indicated.

The primary objective of this research is to evaluate the feasibility and effectiveness of PRC materials in enhancing thermal comfort in low-energy buildings. Specifically, the study aims to: (i) quantify and compare the cooling potential of sky radiators; (ii) evaluate the thermal energy extracted by radiant-capacity ceiling modules (RCM); and (iii) assess system impact on indoor temperatures relative to ambient and control conditions. Additionally, the study develops a practical methodology for the comparative assessment of sky radiator arrays under varying climatic and operational conditions, using multiple-regression models that account for the most influential variables driving the Cooling Potential of Sky Radiators (CPSR). Furthermore, this work compiles and openly releases an extensive experimental database—spanning variations in water flow rate, RCM quantity, and storage volume—to calibrate simulation models, perform sensitivity analyses, and inform component sizing for alternative real-world configurations [31].

2. Methodology

2.1. Full-scale experimental facility

The facility (8.95 m × 7.2 m × 4.2 m) is elevated 0.42 m above ground and hosts two identical test cells with internal dimensions of 5.66 m × 2.68 m × 2.92 m (floor area 15.2 m^2, volume 44.3 m^3), one used as control cell (CC) and the other as experimental cell (EC) (Fig. 1a–c). Walls, roof and floor consist of modular sandwich panels with 0.60 m of Geopannel Classic insulation (λ = 0.034 W/mK), yielding an overall U-value of 0.055 W/m^2K. The highly insulated envelope minimizes heat transfer and decouples indoor conditions from short-term outdoor fluctuations. Each cell has a south-facing, double low-e window (1.87 m^2, U = 1.88 W/m^2K). Further details on envelope and partition properties are given in [28] and in the Supplementary Material, Section S1.

2.2. The radiant-capacitive cooling system (RCCS)

The RCCS builds on the Radiant-Capacitive Heating and Cooling System developed by González and Krüger [11,27], itself inspired by earlier roof-pond concepts integrating evaporative and radiative cooling [32]. In the present work, the concept is implemented as thermally activated building elements (TABs) for radiant cooling, combined with nocturnal and daytime radiative cooling via sky radiators and a water-based thermal storage. This approach is particularly advantageous for both renovation projects and new constructions. Notable characteristics of the proposed system include very low energy consumption, cooling without heating contribution, use of renewable source of cooling power, zero water usage, zero greenhouse gas emissions for operation, improved thermal comfort, and enhanced thermal storage capacity with reduced volume and mass compared to traditional TAB systems [33–35].

The RCCS consists of three main components (Fig. 1d): (i) sky radiators (SRs), positioned to maximize sky view; (ii) indoor Radiant-Capacity Modules (RCMs), installed as ceiling panels; and (iii) a thermally insulated water tank for Thermal Energy Storage (TES). These are connected by a closed-loop hydronic system with controlled flow and three possible circuits. In this study only Circuit 1 was used: water is pumped from the TES through the SRs, then through the RCMs in the EC, and back to the TES. In the radiators, water cools if radiative losses exceed gains; in the RCMs it absorbs heat from the indoor environment, thereby cooling the EC. Further information on RCCS is included in the Supplementary Material, Section S2.

2.2.1. The Sky radiators (SRs)

The SRs are five commercially available polypropylene solar panels [36] (2.0 m × 1.2 m each), with multiple parallel channels connected to polypropylene manifolds. They are mounted on 0.04 m of XPS insulation (λ = 0.032 W/m·K) over 0.015 m OSB panels, on a platform 1.60 m above ground and tilted 8° towards the north (Fig. 2). The panels were installed this way to allow easier access for testing and maintenance, although in practical applications they would typically be placed on the roof to also provide shading from direct solar radiation. Two main configurations were tested: (i) Series A, with the original black polypropylene surface exposed; and (ii) Series B (Fig. 2b), with a 110 μm-thick SpaceCool Silver Film (SSF) [37] adhered to the surface. The SSF is a PRC material with high solar reflectance and high long-wave emissivity, enabling daytime radiative cooling. Additional details concerning the optic characteristics of the sky radiators and the PRC material are provided in the Supplementary Material, Section S3.

Alongside the sky radiators, four material samples measuring 0.20 m × 0.20 m were installed, with their undersides and sides insulated using rigid polystyrene foam. The surface temperatures of these samples (Tr1, Tr2, Tr3, and Tr4) serve as reference temperatures for interpreting the cooling performance of the radiators. The samples include a white-painted metallic sheet (Tr1), a polypropylene panel (Tr2), a polypropylene panel coated with SpaceCool Silver Film (SSF) (Tr3), and an aluminum sheet coated with SSF (Tr4). Notably, the maximum temperature depression of water in the radiators, exposed to the night sky under static conditions (without water flow), correlates with the surface optical and thermal properties of these materials. During the night, the temperature depressions for both the polypropylene panel and the SSF-coated polypropylene panel (Tr2 and Tr3, respectively) are nearly identical.

The optical properties (visible and solar reflectance; emissivity) of the radiator surfaces and reference samples were measured using a portable spectrophotometer and an ET100 emissometer, following UNE-EN 410 [38]. Additional details concerning the optical characteristics of the sky radiators' surfaces and reference samples are provided in the Supplementary Material, Section S4, while Table S2 summarizes the spectral properties of the sample materials.

2.2.2. The Radiant-Capacity Modules (RCMs)

Each RCM (Fig. 2c–d) consists of a 1 mm steel box (0.9 m × 0.9 m × 0.07 m) containing a 3/8″ (9.52 mm) copper coil (9.5 m length) and a water volume of 0.0518 m^3. The thermal capacity of one module is 216.6 kJ/K, about twice that of an equivalent volume of reinforced concrete. Eight RCMs were installed as ceiling panels in the EC, covering 6.5 m^2 (≈43% of ceiling area) with a total water volume of 0.421 m^3. Further details and figures of the RCMs are given in the Supplementary Material, Section S3.

2.2.3. The Thermal energy storage (TES)

The study features two thermally insulated polyethylene water tanks for thermal energy storage (see Supplementary Material, Section S7); TES-1, with a 1000-liter capacity, and TES-2, with a 50-liter capacity. Water circulation is managed by a hydropneumatic system with three circuits and four solenoid valves, all controlled by an automatic system, while the flow rate is regulated by a pressure-regulating valve and a needle valve to maintain stable operations.

2.3. Data acquisition and control system

A Raspberry Pi 4B manages real-time data acquisition and control, connected to NTC modules, PT100 RTDs, thermocouples, a flowmeter, an electric meter, and AC actuators. Variables measured (Fig. 3 and Table S3 in Supplementary Material Section S8) include: water temperatures at SR in/out, RCM in/out, within TES and RCMs; air and globe temperatures in EC and CC; ambient temperature; reference sample temperatures; and water flow rate.

Water and air temperatures at key points were measured with 4-wire PT100 Class A sensors (IEC 60,751); remaining temperatures with T-type thermocouples. Water flow was measured with a Zenner ETWD-M DN15 flowmeter (0–2.5 m^3/h, ±2% accuracy). Apparent sky

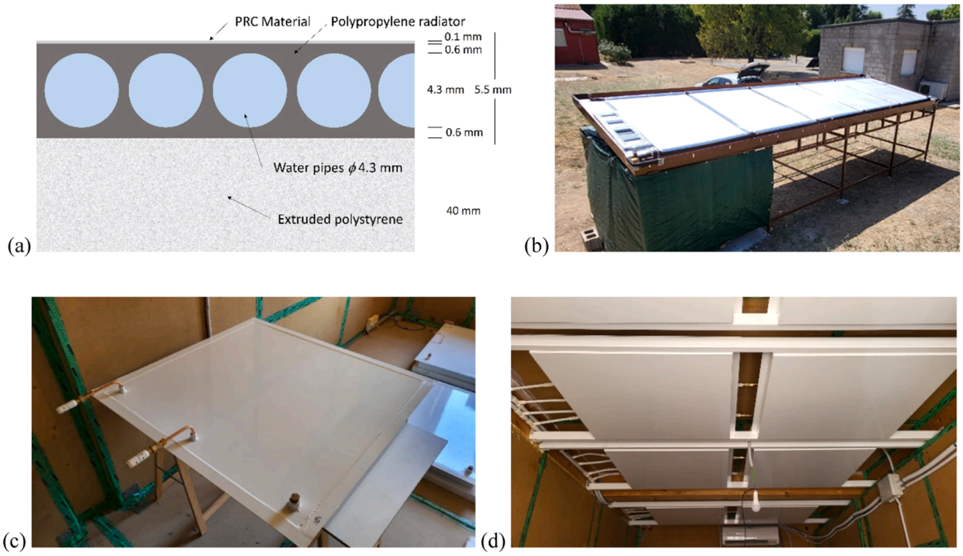

Fig. 2. (a) Dimensions of the cross and longitudinal sections of the sky radiator, on the insulating material. (b) The five polypropylene sky radiators coated with PRC material film. (c) Arrangement of the 8 RCMs mounted on their support structure as ceiling panels, along with their connections to the water inlet and outlet manifolds. (d) Top view of a sealed RCM with inlet, outlet, and water filling connections.

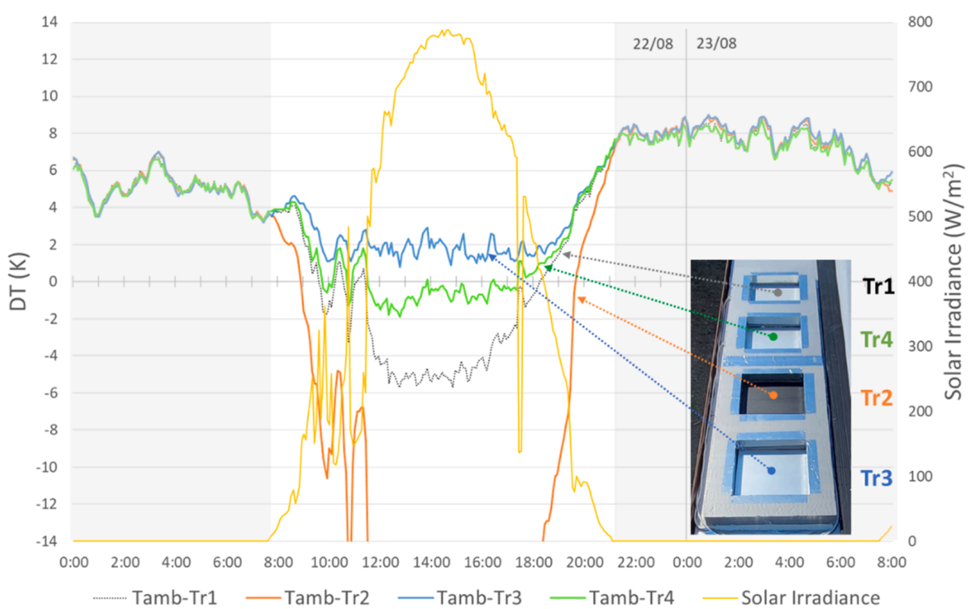

Fig. 3. Difference between ambient air temperature and reference temperatures Tr1–Tr4 along with the irradiance. Data for 22–23 Aug 2024. Tr1: 1 mm steel sheet, painted white. Tr2: polypropylene panel sample. Tr3: polypropylene panel sample coated with SSF material. Tr4: 1 mm aluminum sheet coated with SSF material.

temperature, used as a proxy for sky conditions and precipitable water content [39], was monitored with an Optris CSmicro LT/LTH infrared thermometer. A Davis Vantage Pro2 Plus weather station provided outdoor temperature, humidity, wind, precipitation, solar irradiance and atmospheric pressure.

All temperature sensors were calibrated before installation. Differences between individual sensors and the ensemble mean remained within ±0.15 °C for PT100 probes and ±0.13 °C for thermocouples (standard deviation ≈0.1 °C). Comprehensive information regarding the data acquisition and control system is provided in the Supplementary Material, Section S7

2.4. Experimental program

Nine experimental series (ES) were conducted at the full-scale facility located in Arganda del Rey, Madrid (40°18′50.5″N, 3°28′56.0″W), between late July and late September 2024, a period characterized by frequent heatwaves and daytime outdoor temperatures often exceeding 35 °C and occasionally surpassing 40 °C. Operating conditions were varied systematically to study their influence on system performance: radiator surface (bare polypropylene vs SSF-coated), water flow rate, number of active RCMs, TES volume, and daily operating duration of Circuit 1 (Table 1).

Four series (ES-A1 to ES-A4) were carried out with bare polypropylene SRs (Series A), followed by five series (ES-B1 to ES-B5) with SSF-coated SRs (Series B). In Series A, operation beyond 10 h was found to be counterproductive due to solar absorption of the black panels; therefore, Circuit 1 was operated from 22:00 to 8:00. In Series B, thanks to the highly reflective SSF coating, the system was operated for 12 h (from 21:00 to 9:00) during the first four series, and for 15 h (from 19:00

Table 1
Summary of operating conditions and dates for each experimental series.

Dates	Experimental Series	Circuit-1 (h)	TES (l)	WFR (L/h)	RCM (#)
01/08 - 08/08	ES-A1	10	1000	183	8
09/08 - 12/08	ES-A2	10	1000	387	8
13/08 - 16/08	ES-A3	10	50	396	8
17/08 - 20/08	ES-A4	10	50	380	4
21/08 - 27/08	ES-B1	12	50	363	8
28/08 - 03/09	ES-B2	12	50	170	8
04/09 - 07/09	ES-B3	12	50	158	4
10/09 - 16/09	ES-B4	12	1000	376	8
17/09 - 24/09	ES-B5	15	1000	376	8

to 10:00) in the final series. The purpose of this extended operation was to identify the maximum duration during which the system maintained effective performance, producing water at a temperature suitable for indoor conditioning.

Two distinct target flow rates were tested: a lower rate of ~180 L/h (0.05 L/s, 0.264 L/min·m^2) and a higher rate of ~380 L/h (0.105 L/s, 0.558 L/min·m^2) (actual measured values are reported in Table 1). In seven series, all eight RCMs were active; in two series, only four RCMs were activated to assess the impact on EC temperatures and energy extraction. TES-1 was used in two Series A and two Series B cases, while TES-2 was used in the remaining series, allowing comparison of different storage capacities.

2.5. Performance indicators

Two groups of thermal performance indicators are employed in this study. The first group characterizes the Cooling Potential of the Sky Radiators (CPSR) and quantifies the Energy removed by the Radiant-Capacity Modules (ERCM). The second group examines the effectiveness of internal cooling within the experimental cell by analyzing the temperature depression in the test cell relative to ambient and control cell temperatures. Finally, the relationship between internal temperatures in the EC and the adaptive comfort range will be discussed in terms of the number of hours above the upper limit of the comfort range.

2.5.1. Cooling potential of sky radiators (CP_{SR}, W/m^2)

The cooling potential of the radiators corresponds to the energy dissipated per unit time and per unit area when water is circulated through them. Radiative heat transfer from a radiator exposed to the night sky is primarily influenced by atmospheric thermal radiation and convective exchange with the surrounding air, with a lesser contribution from conduction through the supporting insulation [19]. When water flows in contact with the radiator surface, the water temperature drop between inlet and outlet depends on the inlet fluid temperature, the mass flow rate, and the radiator's surface energy balance. Under solar irradiance, achieving sub-ambient temperatures is more challenging and requires a surface with high solar reflectivity and high thermal emissivity; such conditions can enable daytime radiative cooling.

To quantify the net cooling potential of the sky radiators (CP_{SR}) we calculated an average based on 5-minute records over the entire daily operating period, utilizing the water temperature difference between the radiator inlet and outlet (ΔTw_{SR}) and the water flow rate through it [40], as follows:

$$CP_{SR} = \frac{t}{A_{SR}} \cdot \frac{1}{n} \sum_{i=1}^{n} \dot{m} \cdot c_p \cdot \left(T_{w4,i} - T_{w5,i}\right) \tag{1}$$

Where: CP_{SR} (W/m^2) is the net cooling potential of the radiators per unit area, t (h) is the total measurement period, A_{SR} (m^2) is the total surface area of the SRs, n (every 5 min during t), is the total number of measurements, ṁ (kg/s) is the mass flow rate of water, c_p (J/kg•K) is the specific heat capacity of the water, *Tw4,i* and *Tw5,i* (K) are the inlet and outlet water temperatures at measurement *i*.

2.5.2. Thermal energy removed from the radiant-capacity modules (E_{RCM})

During operation, water cooled in the SRs Flows to the Radiant-Capacity Modules, where it passes through copper-coil heat exchangers and absorbs heat from the water contained in the modules. The cooling water thus enters the experimental cell at temperature Tw6 and leaves at a higher temperature Tw9. The temperature increase of the cooling water (ΔTw_{RCM}) is used to calculate the energy effectively removed from the RCMs, given by:

$$E_{RCM} = t \cdot \frac{1}{n} \sum_{i=1}^{n} \dot{m} \cdot c_p \cdot \left(T_{w6,i} - T_{w9,i}\right) \tag{2}$$

where: E_{RCM} (Wh) is the energy removed from the RCMs, t (h) is the total measurement period, n (every 5 min during t) is the total number of measurements, $\dot{m}$ (kg/s) is the mass flow rate of water, c_p (J/kg•K) is the specific heat capacity of the water, Tw6,*i* and Tw9,*i* (K) are the inlet and outlet water temperatures at measurement *i*.

2.5.3. Temperature depression in the test cell relative to ambient and control cell temperatures

The second group of thermal performance indicators assesses the system's ability to achieve characteristic temperatures—such as daily mean and maximum temperatures—lower than those in the control cell and the outdoor environment. These metrics evaluate the system's cooling effectiveness in maintaining thermal comfort, aiming for temperatures within the adaptive comfort range. For each day of the experimental series, we analyze four quantities: (a) the drop in daily mean temperature of the experimental cell relative to outdoors ($DTavg = Tamb_{avg} - Tec_{avg}$); (b) the drop in daily maximum temperature relative to outdoors ($DTmax = Tamb_{max} - Tec_{max}$); (c) the drop in daily mean temperature relative to the control cell ($DT_{CC\text{-}EC} = Tcc_{avg} - Tec_{avg}$); and (d) the percentage of hours per day meeting the comfort criterion (comfort index, CI).

Comfort Index (CI)

The CI represents the Percentage of time (5-min intervals) per day when the indoor operative temperature in the experimental cell remains below the upper limit of the adaptive comfort range (ULACR). The neutral adaptive comfort temperature (Tn) is calculated following ASHRAE 55 [41]:

$$Tn = 0.31 * Tavg + 17.8 \tag{3}$$

where *Tn* is the neutral temperature and *Tavg* is the 10 day prevailing mean outdoor temperature.

A 90% acceptability band (±2.5 °C) is used; only the upper limit (Tn + 2.5) °C is considered, as the system is designed for cooling. The operative temperature is calculated as the average of the indoor air temperature and the mean radiant temperature in the EC, since the air velocity is below 0.1 m/s [42]. The mean radiant temperature is obtained as a function of the air temperature, the globe temperature (Tg. ec) and the diameter of the globe (d = 0.04 m) [42].

2.5.4. The predictive mean vote (PMV)

The Predicted Mean Vote (PMV) is a widely used thermal comfort index that predicts the average thermal sensation of a large group of occupants on a seven-point scale, from cold (−3) to hot (+3), based on air temperature, mean radiant temperature, relative humidity, air velocity, metabolic rate, and clothing insulation. ASHRAE Standard 55 adopts the PMV as the primary method for evaluating indoor thermal environments, recommending acceptable comfort when the PMV falls within the range of −0.5 to +0.5 and a specified percentage of occupants are satisfied. In this study, the PMV model is applied to the monitored datasets from experimental series A and B to identify the periods during which the system maintained thermal comfort (PMV between −0.5 and +0.5). Calculations were performed using the CBE Thermal Comfort Tool for ASHRAE 55 [43], which ensures consistency with the standard's procedures and facilitates reproducible comfort assessments throughout the experimental periods.

2.6. Regression models

The multiple linear regression method [44] was used to relate the temperature drop across the SRs (ΔTw_{SR} = Tw4 – Tw5) to climatic and operational variables, and thus to predict CP_{SR} under different configurations. After a preliminary correlation analysis and construction of a correlation matrix, the most influential predictors affecting the radiators' thermal balance were selected to build the models.

Regression models were developed for Series B1 and B4 (SSF-coated radiators) and then used to predict ΔTw_{SR} in Series A3 and A2, respectively, which share the same operating configurations. This enabled comparison between measured results with bare radiators and predicted performance if PRC-coated radiators had been used under identical conditions.

3. Results

3.1. On the reference temperatures

Night-time temperatures of the four small reference samples (Tr1–Tr4) are very similar (Fig. 3). The untreated polypropylene panel (Tr2) systematically reaches the lowest stagnation temperatures, consistent with its high emissivity (See Table S2 in Section S6 of the Supplementary Material). Mean offsets with respect to Tr2 are small: +0.05 °C for Tr1, +0.04 °C for Tr4 and +0.17 °C for Tr3, with instantaneous deviations typically within ±0.5 °C.

After sunrise, surface temperatures diverge according to solar reflectance. Tr2 warms rapidly, while the white-painted and SSF-coated samples remain close to their nocturnal values for about one hour. The polypropylene panel coated with SpaceCool Silver Film (SSF) is the only sample that maintains sub-ambient temperatures throughout the day (Fig. 3). This behavior continues as long as the SSF-coated surfaces are kept free of dust or debris, underscoring the importance of maintaining clean radiator surfaces to achieve optimal performance. Accordingly, Tr2 and Tr3 are adopted as reference temperatures for Series A and B, respectively.

3.1.1. Environmental contamination effects during the monitoring period

The long-term performance of PDRC coatings is influenced by environmental aging, dust accumulation and optical degradation. Although long-term reflectance monitoring was not included in the scope of this study and direct start-vs-end solar-reflectance measurements are therefore not available, the experimental data provide indirect evidence of soiling effects. Over the monitoring period, the stagnation temperature of the PDRC-treated reference sample (Tr3) progressively lost its daytime sub-ambient response, and this behaviour was fully recovered after surface cleaning, indicating that dust accumulation reduced performance and that periodic maintenance is required to sustain the radiative-cooling effect. Routine visual inspection and surface-temperature measurements over more than two months did not reveal signs of intrinsic material degradation. Complementary accelerated-ageing data for the same coating, report a solar-reflectance decrease of less than ≈4% after thermal-cycling, humid-heat, wet-freeze and UV-irradiation tests, suggesting modest optical degradation under standard stress protocols [45]. Overall, these results indicate that soiling can affect short-term performance, while long-term optical stability and environmental contamination effects require dedicated studies involving extended monitoring, controlled soiling tests and periodic reflectance/emissivity measurements to define degradation rates and maintenance intervals for real building applications.

3.2. Cooling potential of the sky radiators (CP_{SR})

For each experimental series, CP_{SR} was calculated from 5-min inlet–outlet water temperatures once Circuit 1 reached steady operation (about 20 min after start-up). Tables 2 and 3 summarize average and maximum CP_{SR} and reference temperature depressions (DTr2, DTr3) together with operating conditions.

Across all series, daily mean CP_{SR} values range from 43.4 W/m^2 (ES-B2) to 74.3 W/m^2 (ES-A3), with peak instantaneous values close to 96 W/m^2 (ES-A3 and ES-B4). The mean CP_{SR} over all days is 62.0 W/m^2 for Series A and 52.1 W/m^2 for Series B. Part of this difference arises from the longer operating window in Series B, which includes daytime hours and periods with less favorable climatic conditions.

For Series A, the mean reference temperature depression DTr2 was 6.5 K (maximum of 8.2 K), while DTr3 averaged 5.2 K with peaks of 7.6 K. These values are consistent with the CP_{SR} results, as larger temperature depressions indicate higher cooling potential. In Series B, correlations were moderate and positive (Fig. 4b), whereas Series A exhibited a low and negative correlation (Fig. 4a), suggesting the impact of additional interacting variables and operating conditions.

Daily mean CP_{SR} values and ambient temperatures (Fig. 5) indicate that the highest daily mean CP_{SR} values occur on days when the outdoor minimum temperature drops sharply compared to the previous day. This is linked to larger reference temperature depressions and reveals a strong correlation between CP_{SR} and minimum outdoor temperature. Overall, CP_{SR} consistently increases with lower nighttime minima and decreases when these minima are higher, across all series and operating conditions. CP_{SR} is particularly sensitive to the temperature difference between radiator inlet water and the stagnation temperature of the radiator material: higher inlet temperatures relative to Tr2/Tr3 yield larger cooling potentials through increased radiative and convective heat transfer.

Fig. 6a shows that higher water flow rates systematically increase CP_{SR}, both when all series are grouped and when comparing ES-B1 (≈363 L/h) with ES-B2 (≈170 L/h). Fig. 6b indicates that using the larger TES (1000 L) also leads to higher CP_{SR} than the 50 L tank, because warmer inlet water enhances net heat dissipation, whereas with a small TES the tank cools quickly, reducing temperature differences and thus CP_{SR}.

The analysis shows a strong dependence of CP_{SR} on the temperature difference between the radiator inlet water and the radiator stagnation temperature: larger differences yield higher CP_{SR}. This explains the high peaks in ES-A3 and ES-B4 (84.2 and 84.9 W/m^2). Higher initial water temperatures in the RCMs/TES relative to ambient, together with clear skies, low precipitable water vapor, and lower air temperatures, all enhance radiative cooling potential.

Fig. 7, showing four consecutive days of the ES-B1 series, illustrates the system's dynamics. The reference temperature Tr3 remains below ambient even under high solar irradiance (>800 W/m^2), demonstrating its ability to maintain sub-ambient surface temperatures. Despite non-

Table 2
Average and maximum values of CP_{SR} and DTr in the experimental series A (SR without PRC material). Operating conditions in circuit 1 between 22:00 h and 8:00 h in each series.

Dates	Series	DTr2 (K)		CP_{SR} (W/m^2)		TES	WFR	RCM
		Avg	Max	Avg	Max	(L)	(L/h)	(#)
01/08 to 08/08	ES-A1	**7.6**	10.0	**55.1**	71.2	1000	183	8
09/08 to 12/08	ES-A2	**5.9**	9.5	**63.5**	91.1	1000	387	8
13/08 to 16/08	ES-A3	**6.0**	9.9	**74.3**	95.8	50	396	8
17/08 to 20/08	ES-A4	**6.6**	9.8	**55.1**	66.2	50	396	4

Table 3
Average and maximum values of CP_{SR} and DTr in the experimental series B (SR with PRC material). Operating conditions in circuit 1 between 21:00 h and 9:00 h in B1 to B4 series and between 19:00 h and 10:00 h in B5 series.

Dates	Series	**DTr3** (K)		**CP_{SR}** (W/m^2)		TES	WFR	RCM
		Avg	Max	Avg	Max	(L)	(L/h)	(#)
21/08 to 27/08	ES-B1	**5.4**	8.9	**51.2**	70.6	50	363	8
28/08 to 03/09	ES-B2	**4.1**	9.2	**43.4**	78.3	50	170	8
04/09 to 07/09	ES-B3	**5.7**	10.7	**51.2**	69.5	50	158	4
10/09 to 16/09	ES-B4	**6.4**	8.9	**67.9**	96.2	1000	376	8
17/09 to 24/09	ES-B5	**4.3**	7.9	**47.5**	77.0	1000	376	8

ideal atmospheric conditions, DTr3 ranges from 4.3 to 7.6 °C, with peaks up to 8.9 °C, indicating suitable conditions for radiative cooling. The continuous cooling of water in the radiators and RCMs causes a progressive nighttime decrease in the experimental cell (Tec) air temperature and also enables daytime heat removal. As a result, Tec remains on average 3 °C below ambient and 6.6 °C below the control cell temperature (Tcc), confirming the system's capacity to reduce indoor temperature peaks and maintain thermal comfort (Fig. 7).

Fig. 8 shows the evolution of radiator inlet and outlet water temperatures during operation (21:00–09:00) for the night of August 22–23 (ES-B1). At the start of circuit-1, Tamb exceeds 30 °C while TES-2 water is close to Tr3; temperatures stabilize within 20–30 min with $\Delta Tw_{SR} \approx$ 1.4 K, increasing to about 1.9 K as Tamb decreases and Tr3 reaches its maximum depression. The inlet–outlet difference, reflecting net longwave radiative losses plus convection, is enhanced under the favorable conditions of this night (average DTr3 = 7.6 K), especially after 02:00 h when air temperature falls below the radiator surface temperature.

A quantitative evaluation of the mounting configuration (1.6 m height, 8° tilt) shows that ground-reflected shortwave and ground-emitted longwave radiation contribute negligibly to the measured CP_{SR}. For an 8° tilt, the absorbed ground-reflected solar irradiance is <1 W/m^2 even under DHI = 1000 W/m^2, and <0.05 W/m^2 under the irradiance levels encountered during ES-B1–B5. Longwave exchange is similarly negligible: the ground view factor is ≈0.005, yielding ≈1 W/m^2 even for a 50 °C black-body ground. These results are further reinforced by the coating's spectral and angular properties, which strongly suppress both shortwave and longwave contributions at grazing incidence. Regarding convection, the small vertical separation between the rooftop anemometer and the radiators (≈3 m), together with the low water–air

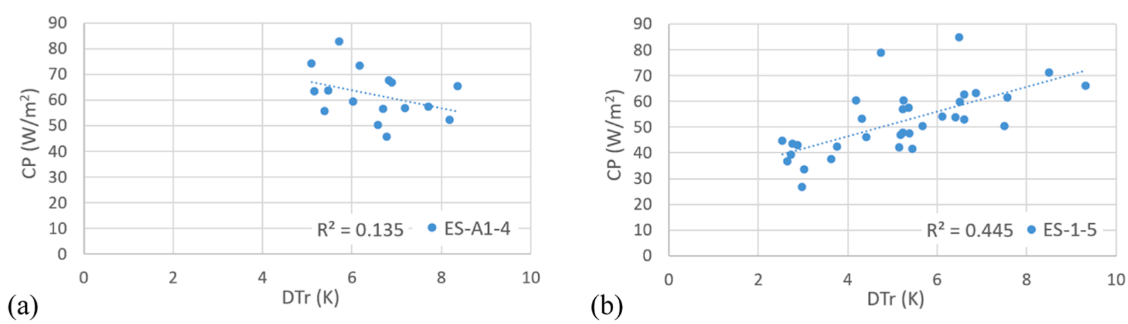

Fig. 4. a. Correlation between the reference temperature depression (DTr2) and the cooling potential in series A (a); b. Correlation between DTr3 and CP_{SR} in series B.

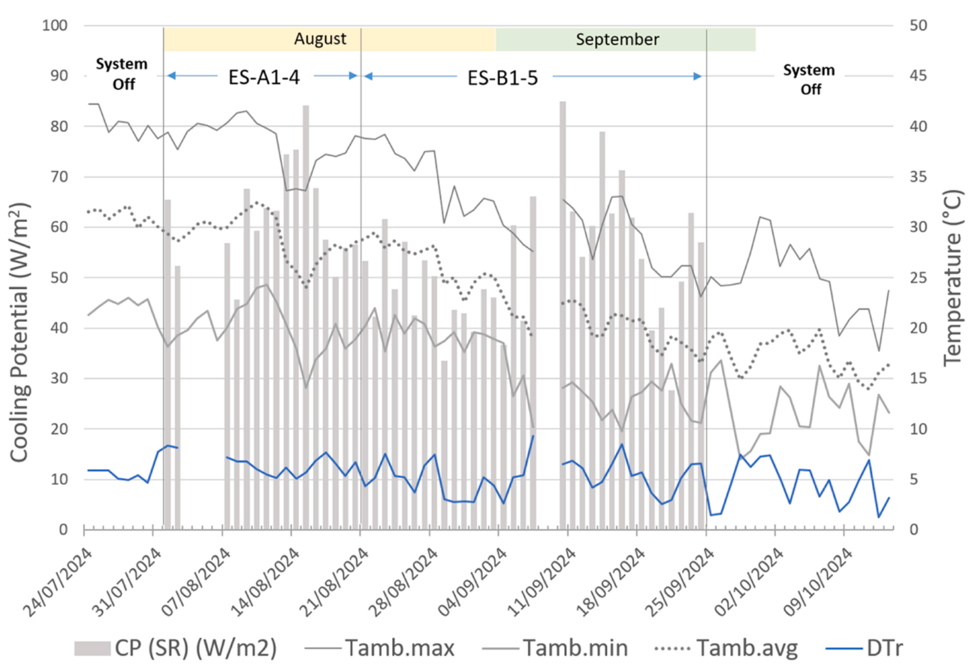

Fig. 5. Daily mean CP_{SR} values for each experimental series and their relationship with the ambient air maximum, mean, and minimum temperatures, as well as with the corresponding reference temperature depression.

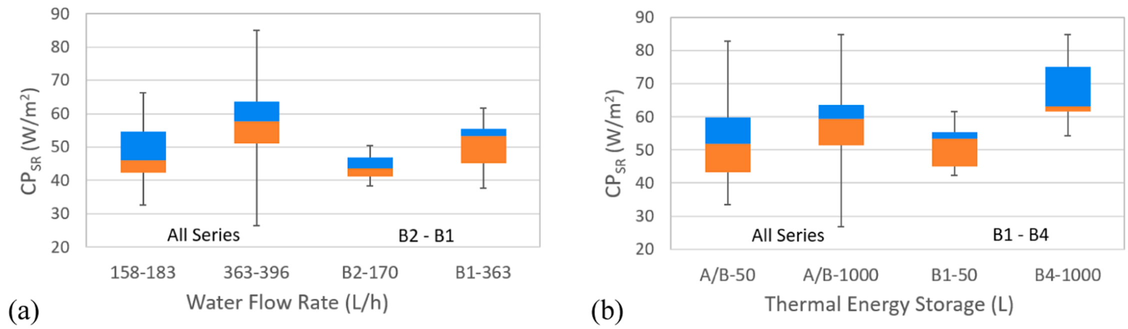

Fig. 6. (a) Box plot illustrating the relationship between water flow rates and corresponding PC_{SR} values, comparing all experimental series categorized into two water flow groups, along with data from series B1 and B2 (B1 = 363 L/h; B2 = 170 L/h). Higher flow rates are associated with a distinct increase in cooling potential. (b) Boxplot of daily mean CP_{SR} values showing consistently higher CP_{SR} for the 1000 L TES compared to the 50 L TES, for both the complete dataset and for series B1 and B4 (B1 = 50 L; B4 = 1000 L).

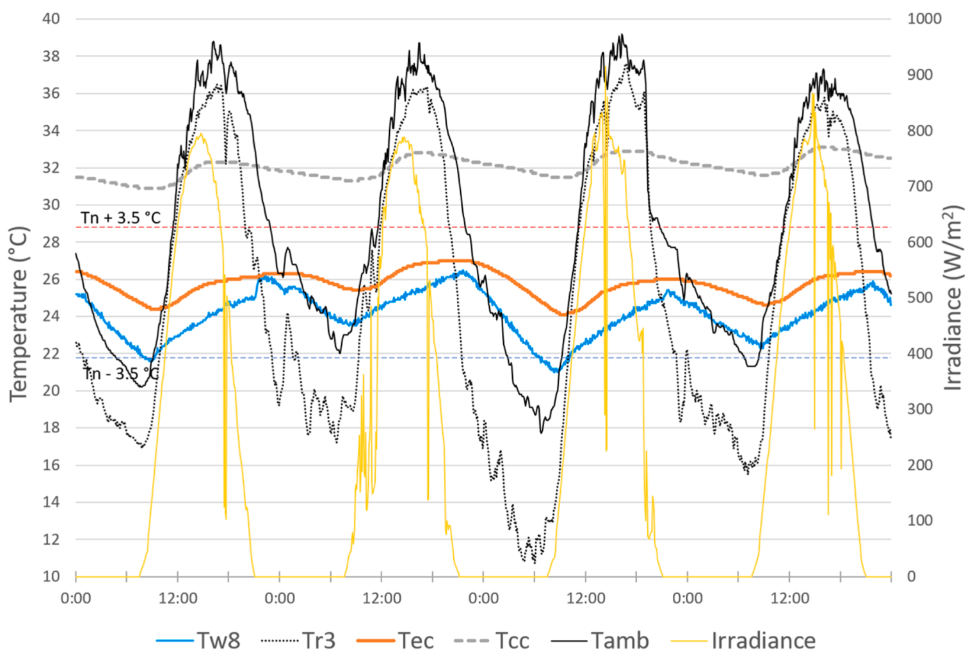

Fig. 7. Measured temperatures in control cell (Tcc), experimental cell (Tec), ambient (Tamb), reference (Tr3), and water in the RCMs (Tw8), along with irradiance values, over four days of ES-B1 (TES-2, 363 L/h and 8 RCM), from August 12 to August 24, 2024.

temperature differences observed (≤3 °C), indicates that uncertainties from local convective disturbances are minor relative to radiative effects. Overall, the mounting configuration is not expected to introduce significant bias in the reported CP_{SR} values.

3.3. Thermal energy removed from the radiant-capacity modules (E_{RCM})

Daily E_{RCM} values, derived from the 5-min inlet–outlet temperature difference across the RCMs (ΔTw_{RCM}), are shown in Fig. 9, along with the corresponding maximum, average, and minimum ambient temperatures, as well as the mean temperatures of the control and experimental cells. Statistical analysis of the results indicates that the average E_{RCM} value for Series B is 3240 Wh/day (494 Wh/m^2.day), approximately 14% higher than the average obtained for Series A (2840 Wh/day (432 Wh/m^2.day)). However, it is important to note that, for the same values of CP_{SR}, the difference between Series A and B is considerably greater, as illustrated in Figure 10(a).

The correlation between CP_{SR} and E_{RCM} (Fig. 10a) highlights the effect of radiator surface material: for the same CP_{SR}, Series B (SSF-coated radiators) removes substantially more energy from the RCMs than Series A. Trend lines indicate that at CP_{SR} = 50 W/m² and 60 W/m², ERCM in Series B exceeds Series A by ~92% and ~44%, respectively.

The relative influence of water flow on the energy removed in Series B is shown in Fig. 10b. At lower flow rates of 0.23–0.25 L/min·m² (160–180 L/h), Series B2 and B3 exhibit higher E_{RCM} values than those observed in Series B1, B4, and B5, where the flow rate is 0.55 L/min·m² (376 L/h).

The effect of water flow rate is clearly observed when comparing the trend lines for Series B1 and B2 in Fig. 10c. In Series B1, with a flow rate of 365 L/h, the E_{RCM} at a CP_{SR} value of 50 W/m² is approximately 69% of that corresponding to Series B2, which operates at a flow rate of 158 L/h (0.23 L/min·m^2).This observation is consistent with the numerical simulations of Forte et al. (2025) [31], which—using the experimental data generated in the present work—indicate that a water flow rate in the range 0.2–0.3 L/min·m^2 (with an optimal trade-off near 0.23–0.25 L/min·m^2) maximizes the energy removed from the RCMs for the SR surface and configuration used in this study.

In contrast to CP_{SR}, the results clearly show that lower water flow rates lead to higher energy removal, highlighting the inverse relationship between water flow rate and effective cooling energy in this configuration.

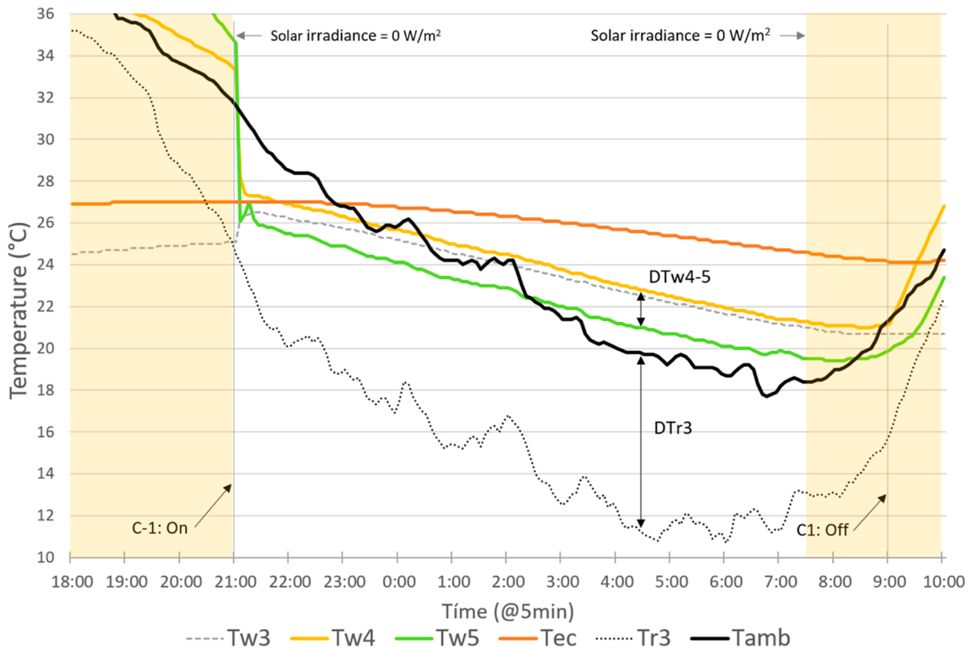

Fig. 8. Radiator inlet (Tw4) and outlet (Tw5) temperatures, along with ambient (Tamb), experimental-cell (Tec), and reference (Tr3) temperatures corresponding to the night between August 22 and 23, 2024, in ES-B1. The hours with solar irradiance exceeding 0 W/m² are also indicated.

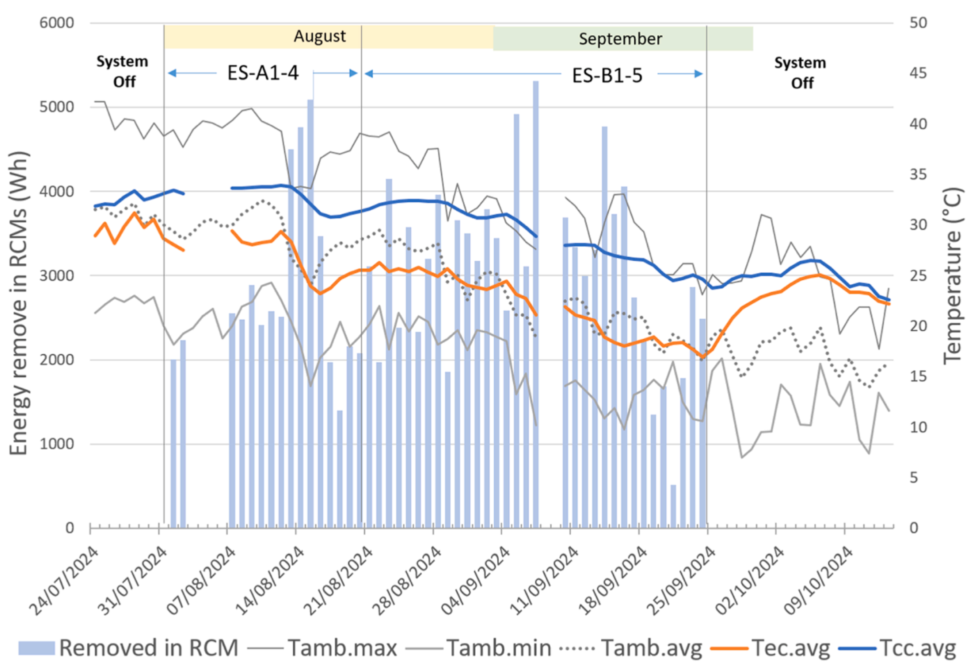

Fig. 9. Daily energy removed values for each experimental series and their relationship with the ambient air maximum, mean, and minimum temperatures, as well as with the corresponding reference temperature depression.

TES volume also affects E_{RCM} (Fig. 10d). With TES-2 (50 L, ES-B1), a larger fraction of the available cooling capacity is used to cool the RCMs, yielding higher E_{RCM} for a given CP_{SR} than with TES-1 (1000 L, ES-B4), where a much larger water mass must be cooled.

Fig. 10e–f compares configurations with and without SSF under similar operating conditions. In both cases, SSF-coated radiators (Series B1 and B4) achieve higher E_{RCM} than bare polypropylene (Series A3 and A2), confirming the advantage of PRC surfaces when the full day–night cycle is considered.

The interaction between water flow rate, residence time, and radiative heat dissipation plays a central role in the thermal performance of the RCCS. For identical climatic conditions and system configuration, the flow rate determines the temperature evolution of the circulating water and therefore affects both the instantaneous cooling power of the sky radiators (CP_{SR}) and the daily extracted cooling energy from the RCMs (E_{RCM}).

When the inlet water temperature to the SRs differs—for example, 25 °C in one case and 20 °C in another—the SRs will deliver different outlet temperatures and consequently different CP_{SR} values. The case with the higher inlet temperature exhibits a higher instantaneous CPSR because the radiative heat flux increases with the temperature difference between the radiator surface and the sky. However, the outlet water

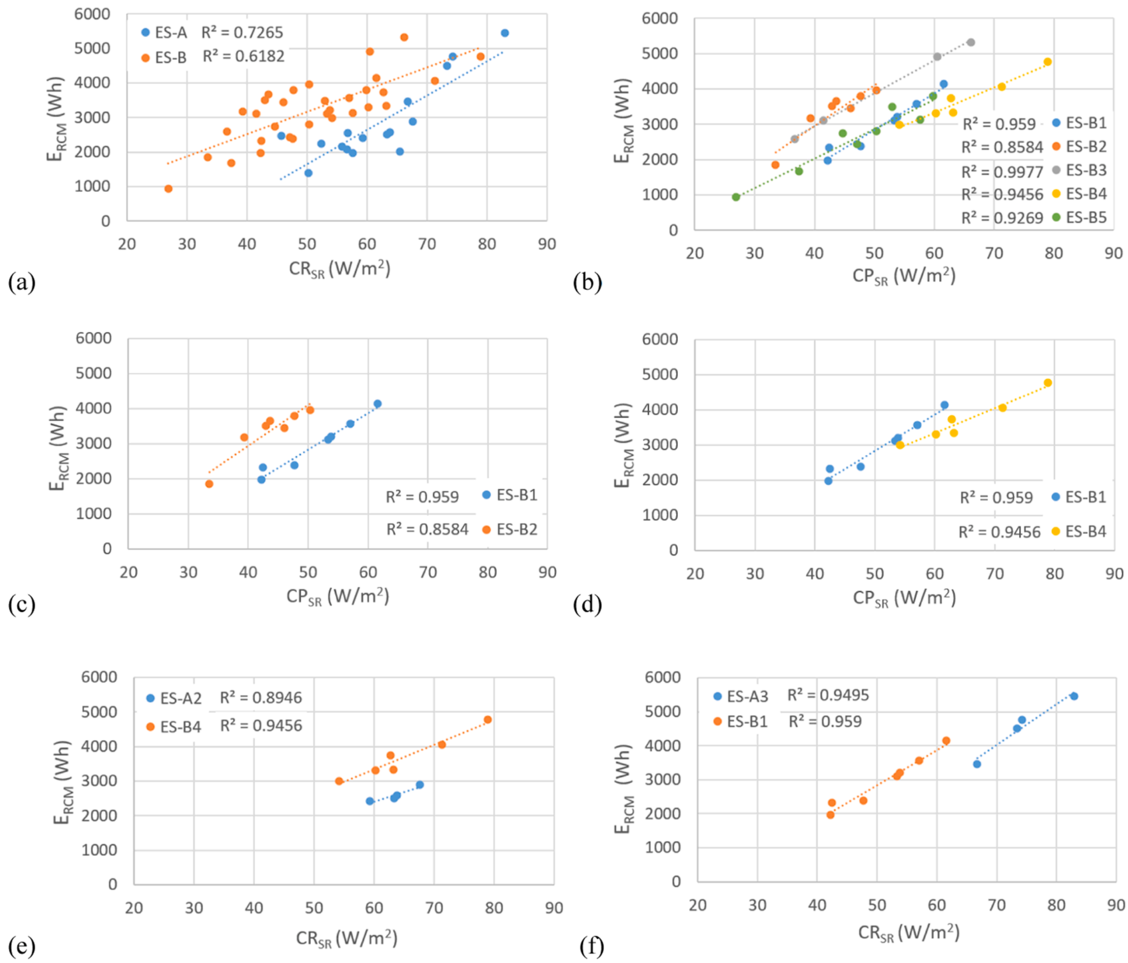

Fig. 10. Correlations between the cooling potential of the sky radiators and the energy effectively removed in the RCMs. (a) Effect of the radiator surface on the performance differences between Series A and B. (b) Effect of water flow rate in Series B. (c) Effect of water flow rate between Series B1 and B2. (d) Effect of storage water volume between Series B1 and B4. (e) Effect of radiator material between Series B4 and A2. (f) Effect of radiator material between Series B1 and A3.

temperature in this case remains higher, which reduces the temperature gradient available for heat extraction in the RCMs.

If both cases start from the same initial inlet water temperature in the RCMs, the configuration with the lower outlet temperature from the SRs (i.e., the lower-temperature inlet case) enables a larger E_{RCM} over the full cycle, provided that the flow rate is sufficient to maintain continuous heat removal. This behavior is consistent with the optimal range of 0.2–0.3 $L{\cdot}min^{-1}{\cdot}m^{-2}$, as identified by Forte et al. [31].

A similar mechanism appears when comparing two different flow rates under identical inlet temperatures. Lower flow rates increase the residence time of water in the SRs, allowing the water to cool more effectively and reach outlet temperatures that may fall below ambient air temperature under favorable radiative conditions. In this regime, convective heat transfer from the ambient air becomes a heat gain rather than a loss, but the net radiative cooling remains dominant. The resulting lower outlet temperature enhances the RCMs' ability to extract heat, increasing E_{RCM} even though CP_{SR} is reduced.

In contrast, higher flow rates reduce residence time, limiting the temperature drop in the SRs. The outlet water temperature remains closer to ambient, which diminishes the RCMs' cooling capacity but increases CP_{SR} due to the higher radiator surface temperature.

Overall, the coupled heat-transfer dynamics indicate that lower flow rates favor daily energy extraction in the RCMs, while higher flow rates enhance instantaneous radiative cooling in the SRs. The optimal engineering compromise for the prototype studied here lies between 0.2 and 0.3 $L/min{\cdot}m^2$, where the balance between SR radiative performance and RCM heat extraction is maximized.

3.4. *Characteristic temperatures*

Table 4 summarizes daily average and maximum temperatures and swings in the ambient, control and experimental cells, as well as key performance indicators: DTavg, DTmax and $DT_{CC–EC}$.

In the EC, the RCMs installed as ceiling panels maintain lower surface temperatures than the surrounding enclosure, enabling continuous heat removal; the water cooled during circuit-1 operation kept the EC's average indoor temperature below outdoors for most of the monitoring period (Table 4, Figs. 11,12), as reflected by DTavg. For Series A, DTavg ranged from 0.3 to 3.2 K (mean ≈ 2.0 K), while for Series B it ranged from −1.8 to 2.6 K (mean ≈ 0.5 K) (Fig. 12a). Due to the high thermal inertia of both cells, indoor temperatures respond more slowly than outdoors, so rapid day-to-day drops in ambient temperature can reduce or even reverse DTavg, whereas sequences with small outdoor variations reveal the clearest sub-ambient cooling. The daily mean temperature difference between CC and EC ($DT_{CC–EC}$) highlights the system's effect, with Series B achieving greater overall cooling than Series A (7.0 K vs. 5.9 K; Fig. 12b). Daily maximum temperature reductions ranged from 7.3 to 12 K in Series A and from 7.6 to 11.2 K in Series B, generally increasing with higher outdoor maximum temperatures.

3.4.1. *On the comparison of RCM surface temperature and dew point*

Fig. 13a and 13b show the temperature differences between the RCM

Table 4
Summary of characteristic temperatures and thermal performance indicators of the cooling system in experimental series A and B.

Series	Ambient			Control Cell			Experimental Cell			Performance Indicators		
	Avg (°C)	Max (°C)	Swing (K)	Avg (°C)	Max (°C)	Swing (K)	Avg (°C)	Max (°C)	Swing (K)	DTavg (K)	DTmax (K)	DT_{CC-EC} (K)
A1	29.8	39.7	19.9	33.5	33.9	0.9	28.3	29.4	2.1	1.4	10.3	5.2
A2	31.8	40.2	16.9	33.8	34.4	1.2	28.5	29.4	2.0	3.2	10.8	5.3
A3	25.7	34.4	17.1	32.5	33.0	1.0	25.4	27.1	3.0	0.3	7.3	7.1
A4	28.0	37.7	18.9	31.0	31.7	1.3	24.8	25.7	2.0	3.2	12.0	6.2
B1	28.2	37.7	17.4	32.2	32.9	1.4	25.6	26.5	1.9	2.6	11.2	6.6
B2	24.9	33.0	14.2	31.6	32.2	1.3	24.6	25.4	1.8	0.3	7.6	6.9
B3	21.0	28.9	14.6	30.0	30.8	1.5	22.9	24.0	2.3	−1.8	4.9	7.2
B4	21.7	30.5	16.8	28.0	29.1	2.0	21.1	22.0	2.1	0.6	8.6	6.9
B5	19.3	27.7	13.8	26.1	26.9	1.5	18.5	19.2	1.6	0.8	8.5	7.6

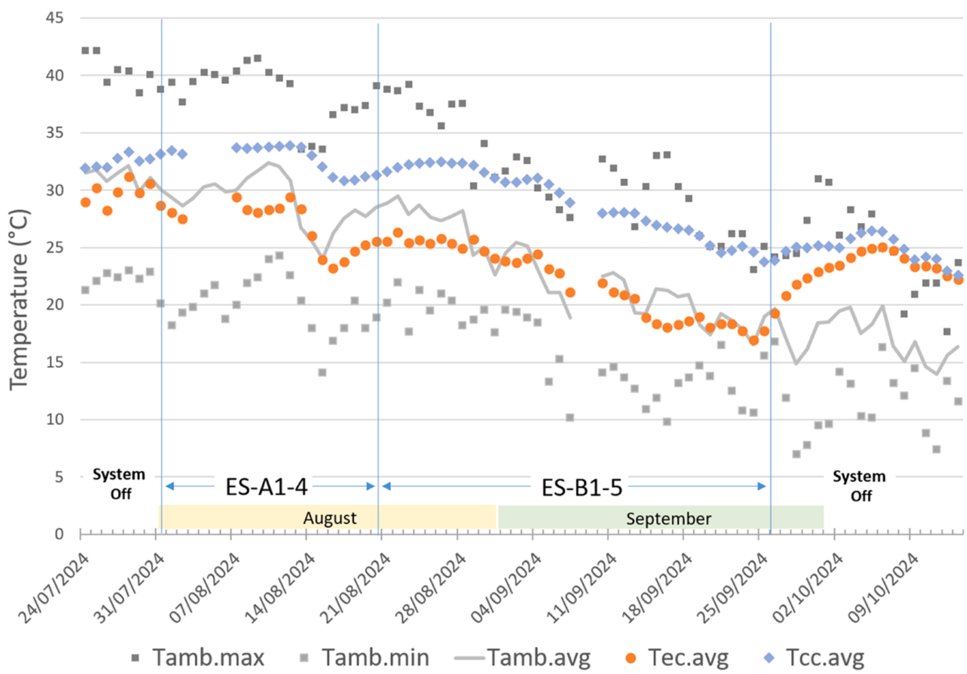

Fig. 11. Daily average temperature in the control and experimental cells for each experimental series, and its relationship with the ambient air maximum, mean, and minimum temperatures.

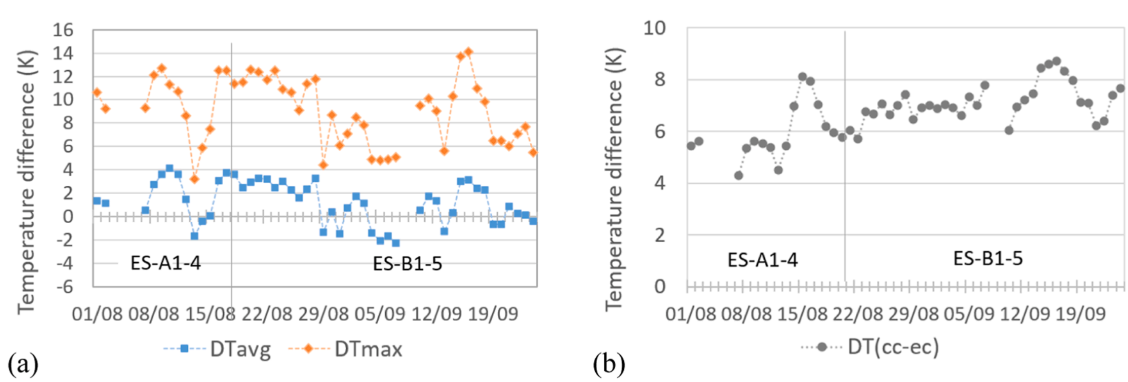

Fig. 12. Characteristic temperatures: (a) Temperature differences (DTavg) between the daily ambient mean and maximum temperatures and the Experimental Cell (EC) daily mean and maximum temperatures; (b) DT_{CC-EC}, the difference between the daily mean air temperatures of the two test cells.

surface and the dew point for Experimental Series A and B, respectively. For Series A (12 monitored days of the four experimental series) the temperature difference (Tsurf − Tdp) ranged from 4.9 °C to 22.5 °C, with an average of 13.3 °C. These margins are well above saturation conditions, indicating that condensation on the RCM surfaces did not occur during Series A.

For Series B (37 monitored days), the Tsurf − Tdp difference ranged from 0 °C to 22.5 °C, with a mean value of 8.4 °C. Only 1.8% of the Series B data show differences between 0.02 °C and 1.0 °C, while the remaining 98.2% exceed 1.0 °C. We observed a clear relationship with outdoor

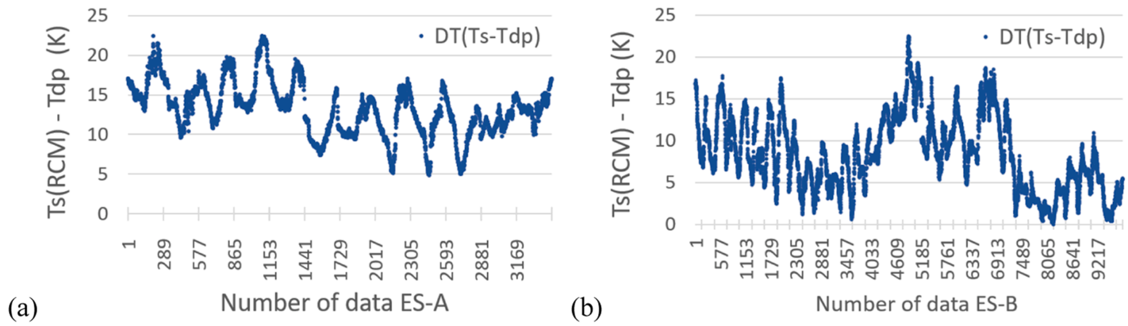

Fig. 13. Temperature difference between the RCM surface and the dew point for the two experimental series: (a) ES-A; (b) ES-B.

relative humidity: higher external RH corresponds to smaller Tsurf − Tdp differences and occasional values approaching 0 °C. It is important to emphasize that these results were obtained under continuous-operation experimental conditions that maximize cooling availability; in practical applications, the automatic control strategy would prevent persistent overcooling of the RCMs by adjusting setpoints, so the marginal low-difference instances observed in Series B would be avoided.

Regarding possible condensation on the radiators' emissive surface, [31] report parametric simulation results for the present system applied to dwellings in Madrid and Rome, stating that "the impact of condensation remains limited… The seasonal occurrence of condensation is below 0.03% of the total operational time in Madrid, and approximately 0.3% in Rome."

3.5. Thermal comfort analysis

3.5.1. Adaptive model

Table 5 reports, for each series, the percentage of time during which the EC operative temperature stays below: (i) the upper limit of the adaptive comfort range (ULACR, ASHRAE 55), and (ii) a fixed upper limit of 27 °C (Spanish INSHT criterion). It also includes the corresponding neutral temperature (Tn), ULACR and 10-day running mean temperature (Tmean).

Using ULACR, Series B maintains comfort 100% of the time across all monitored days. Series A2, A3 and A4 also show virtually full compliance, while ES-A1 falls slightly below 100% due to residual effects during the first hours. Overall, even with outdoor maxima up to 41.5 °C, indoor conditions remain within the adaptive comfort range almost continuously.

Under the fixed 27 °C limit, ES-A1 and ES-A2 only achieve 62.4% and 0% compliance, respectively, whereas all remaining series reach 100%. This reflects the more stringent nature of the fixed limit compared to the adaptive criterion under very hot conditions, and highlights the importance of using context-appropriate comfort models.

Table 5
Summary of the calculated percentage of time within thermal comfort index (CI) for each experimental series (A and B), together with the average ambient (Tamb) and EC (Tec) temperatures. The neutral temperature (Tn), the upper limit of the adaptive comfort range (ULACR), and the 10-day running mean temperature are also included (Tmed).

Series	CI		Tec	Tamb	Comfort Parameters		
	ULACR (%)	UL 27 (°C)	Avg (°C)	Avg (°C)	Tn (°C)	ULACR (°C)	Tmean (°C)
A1	94.3	62.4	28.3	29.8	27.0	29.5	29.7
A2	99.8	0	28.5	31.8	26.9	29.4	29.5
A3	97.8	100	25.4	25.7	27.0	29.5	29.7
A4	100	100	24.8	28.0	26.8	29.3	29.1
B1	100	100	25.6	28.2	26.4	28.9	27.8
B2	100	100	24.6	24.9	26.5	29.0	28.2
B3	100	100	22.9	21.0	25.8	28.3	25.8
B4	100	100	21.1	21.7	25.1	27.6	23.6
B5	100	100	18.5	19.3	24.4	26.4	21.2

3.5.2. Predicted mean vote PMV/PPD

The Predicted Mean Vote (PMV) was computed hourly for 12 days of Experimental Series A and 37 days of Experimental Series B using the CBE Thermal Comfort Tool for ASHRAE 55 (Tartarini et al., 2020). Measured inputs were indoor air temperature, indoor relative humidity, and mean radiant temperature; estimated inputs were air speed (0.1 m/s), metabolic rate (1.0 met), and clothing insulation (0.5 clo, typical summer indoor clothing). Note that outdoor peak temperatures during Series A reached 37–42 °C, whereas in Series B peak outdoor temperatures were 35–40 °C only for the first nine days and then decreased progressively to about 25 °C for the remainder of the campaign; these external conditions influenced the cooling demand and observed PMV distributions.

For Series A (Fig. 14a) the hourly PMV distribution shows 35.2% of hours within the neutral band (−0.5 to +0.5), 30.6% slightly warm (+0.5 to +1.0), 1.0% above +1.0, and 33.2% below −0.5 (slightly cool/cool). Applying the system's automatic control logic — stopping Circuit 1 to prevent further cooling of the RCMs and switching to Circuit 3 so SR-cooled water maintains TES temperature — would avoid the lower excursions; under that control strategy the operative outcome for Series A is approximately 68.5% neutral and 31.5% slightly warm.

Series B (Fig. 14b) yielded 31.2% neutral hours and 68.8% of hours with PMV < −0.5, indicating the system often overcools the conditioned space under the monitored operating schedule. Crucially, observing PMV values below −0.5 in either series should not be interpreted as a failure of the cooling system; rather, it demonstrates the system's capacity to exceed cooling requirements. In practical application, setpoints and the automatic control algorithm would be adjusted to prevent persistent overcooling, thereby ensuring neutral thermal conditions for essentially 100% of operating time while avoiding unnecessary energy use.

3.6. Multiple regression models

The development of the multiple regression model for ES-B4 and its application to the ES-A2 data is presented here. The development of the multiple regression model for ES-B1 and its application to the ES-A3 data is provided in Supplementary Material, Section 9.

3.6.1. ES-B4 model

To develop the multiple regression model for ES-B4, four independent variables have been selected, as previously indicated in Section 2.6. A correlation matrix was used to analyze the degree of association between the temperature difference of the water at the radiator inlet and outlet (ΔTw_{SR}) and the seven candidate variables: Tamb, Tsky, Tr3, Tw4, RH, Tw4−Tr3, and Tamb−Tr3. The correlation matrix reveals that ΔTw_{SR} is strongly correlated with Tr3 (r = –0.74) and Tsky (r = –0.72), while its association with Tamb is moderate (r = –0.69). In addition,

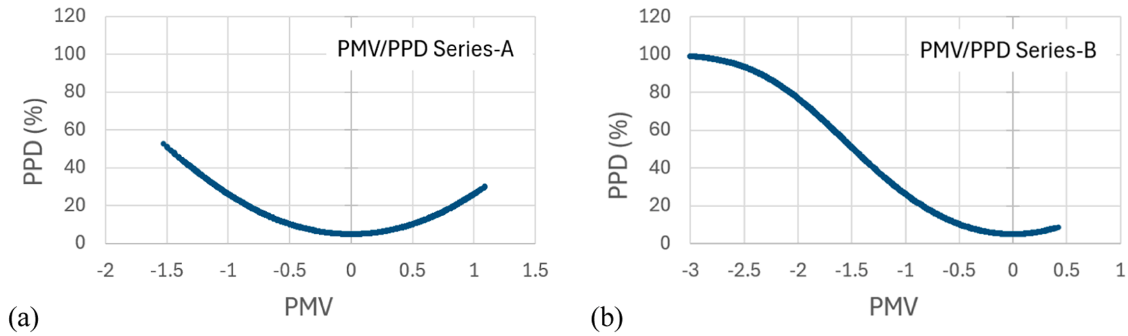

Fig. 14. Predicted Mean Vote (PMV) and Percentage of People Dissatisfied (PPD): (a) Experimental Series A, (b) Experimental Series B.

Tw4–Tw5 shows a strong positive correlation with Tw4–Tr3 (r = 0.83). Conversely, Tamb and Tr3 are highly correlated (r = 0.86), indicating a substantial degree of redundancy among these temperature variables.

Despite the strong correlation between Tamb and Tr3, Tamb was retained in the model because of its interpretative relevance and consistency with the context of the study. Its inclusion contributes to a more comprehensive understanding of the system's thermal dynamics, providing complementary information that may not be fully captured through Tr3 alone. In this case, the results of the multiple linear regression also show that the four predictors are highly significant, with p-values well below 0.001. Their 95% confidence intervals do not include zero, thus justifying their inclusion in the final model.

It is important to note that certain climatic variables highly relevant to radiative cooling—specifically atmospheric precipitable water vapor and conventional cloud-cover indices—were not directly available during the monitoring period. However, sky infrared temperature (Tsky) closely reflects atmospheric water content and cloud presence [39], so using Tsky as a predictor effectively captures much of the radiative impact of PWV and cloud passages; scalar cloud-cover metrics are often ambiguous because they omit cloud altitude/type/temperature. Wind speed was not recorded in the immediate vicinity of the radiators and therefore was excluded as an explicit predictor; its influence is expected to be implicit in the stagnation temperatures Tr2 and Tr3. To check this assumption, we computed the correlation between roof-level wind speed and ΔTw4–5 for the first four days of ES-B4 and obtained $R^2 = 7.62 \times 10^{-7}$, confirming that the available wind data provided no explanatory power for the dependent variable.

The purpose of the multiple linear regression models developed in this study is not to predict RCCS performance under arbitrary climatic conditions, but rather to provide a consistent statistical framework for comparing experimental series conducted at different times, where climatic variability is unavoidable. A model calibrated on one series and validated internally enables meaningful cross-comparison with another series in which a specific operational parameter was modified. Broader generalization to different climatic regimes requires a dedicated simulation approach, which is addressed through the numerical model developed in Forte et al. [31].

Based on these considerations, a multiple regression model was developed using on the first four nights of ES-B4. Tr3, Tsky, Tamb, and Tw4–Tr3 were again selected as predictors because they show the strongest relationships with ΔTw_{SR}. The resulting model is expressed as follows:

$$\Delta TwSR(B4) = 0.24725 - 0.13482 * Tamb - 0.02919 * Tsky + 0.16729 * Tr3 + 0.15197 * (Tw4 - Tr3) \tag{4}$$

With $R^2 = 0.9446$; RMSE = 0.119 °C. This model was validated against data of the last three nights of the experimental series B4 (Fig. 15), yielding a result of: $R^2 = 0.8893$.

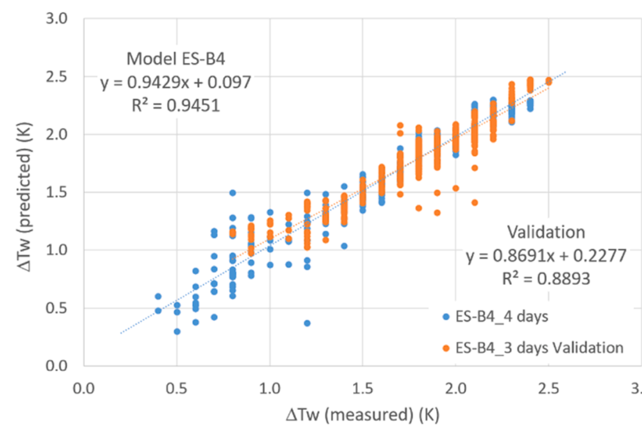

Fig. 15. ES-B4 model validation. ΔTw_{SR} measured vs. predicted.

3.6.2. *B4–A2 application model. Comparative analysis of cooling potential (CP_{SR})*

The regression model developed for ES-B4 was applied to ES-A2, to estimate CP_{SR} that would have been obtained if SSF-coated radiators had been used under identical operating conditions.

ES-B4 and ES-A2 share TES-1 (1000 L) and 8 RCMs, with nearly identical flow rates (376 vs. 387 L/h). The measured average CP_{SR} is 63.8 W/m² for ES-A2 and 68.1 W/m² for ES-B4. When the ES-B4 model is applied to ES-A2 data, the predicted CP_{SR} rises to 77.0 W/m², ~12% higher than the measured value in ES-B4. This suggests that, under similar climatic conditions, PRC-coated radiators combined with large TES would offer improved thermal performance relative to bare polypropylene radiators.

Overall, nighttime performance of polypropylene radiators with and without PRC coating is similar, as both surfaces have comparable emissivity and yield almost identical nocturnal stagnation temperatures (Tr2 ≈ Tr3). However, the PRC coating clearly extends the effective cooling period into daytime. Based on the experimental series, SSF-coated radiators are estimated to provide an additional 2–4 h/day of useful cooling, depending on weather conditions, thereby increasing daily heat removal from the system.

4. Discussion

The experimental results demonstrate the effectiveness of the Radiant-Capacity Cooling System (RCCS) in maintaining sub-ambient and thermally comfortable indoor conditions under hot summer climates. The analysis of reference temperatures confirmed that both polypropylene and SSF-coated radiator materials achieved comparable nocturnal surface temperatures under stagnation conditions, with the uncoated polypropylene panel (Tr2) reaching slightly lower temperatures. However, during daytime exposure, the SSF-coated surfaces exhibited a stronger capacity to maintain sub-ambient temperatures, emphasizing the importance of high solar reflectivity and surface cleanliness for maximizing radiative cooling potential.

The cooling potential of the sky radiators (CP_{SR}) was shown to depend primarily on the temperature difference between the radiator inlet water and the radiator surface stagnation temperature. The daily average CP_{SR} values for each experimental series ranged from 43.4 to 74.3 W/m^2, with instantaneous peaks exceeding 95 W/m^2. The experimental series revealed that higher thermal storage volumes and warmer inlet water temperatures increased CP_{SR}, as these conditions enhanced the driving temperature difference between the water and the sky radiator surface. However, the radiative cooling efficiency was ultimately limited by climatic factors, such as the minimum ambient temperature and the sky emissivity. The strong correlation between CP_{SR} and daily minimum ambient temperature indicates that the system's cooling potential increases under clearer, drier atmospheric conditions.

While higher water flow rates and larger ΔTw_{SR} increase instantaneous cooling power, the outlet water temperature is only useful for indoor cooling when it falls below a target threshold (e.g. the adaptive neutral temperature) and below the RCM water temperature. This underlines the interest of operating on stored cold water (TES) for daytime cooling, for example via Circuit 2, which will be addressed in future work.

The energy effectively removed from the Radiant-Capacity Modules (E_{RCM}) confirms the system's capacity to store and deliver meaningful cooling energy to the indoor environment. Series B achieved on average 3.24 kWh/day (432 Wh/m^2•day), 14% more than Series A, mainly due to the use of the SSF material coating and extended operating hours. Lower water flows (0.23–0.25 L/min·m^2) increased E_{RCM}, in line with previous modelling results that indicate an optimal range where residence time in the RCMs is sufficient for effective heat exchange [31]. Conversely, in Circuit-1 operation, a larger TES volume reduced instantaneous E_{RCM}, since the cooling capacity must be distributed over a much greater water mass.

Indoor temperature data confirm that the RCCS mitigates both mean and peak temperatures in the experimental cell (EC). Mean temperature differences between control and experimental cells (DT_{CC-EC}) of 5.9 K (Series A) and 7.0 K (Series B), together with reductions of 7–12 K in daily maximum temperatures, provide substantial relief during heat waves and are highly relevant for passive or low-energy cooling strategies.

From a comfort standpoint, the RCCS kept the operative temperature below the upper limit of adaptive comfort (ULACR) for almost 100% of the monitored time, even when outdoor maxima reached 41.5 °C. Under the more stringent fixed 27 °C limit, all series except the first two A-series tests also achieved full compliance. These results demonstrate that the system can maintain indoor comfort without conventional mechanical cooling under severe summer conditions. The PMV/PPD results further clarify the comfort implications of the RCCS under the monitored operating schedule. In both experimental series, the system maintained indoor conditions generally close to thermal neutrality, although the fixed circulation timetable led to recurrent slightly-cool conditions, particularly in Series B as outdoor temperatures declined. These deviations reflect excess cooling capacity rather than a limitation of the system, and highlight the sensitivity of PMV to small operative-temperature reductions. The contrast between Series A and B also illustrates how varying external loads shape comfort outcomes. Overall, the PMV/PPD analysis reinforces the need for adaptive control to better match cooling output to real-time comfort requirements.

Finally, the multiple regression models developed for Series B1 and B4 ($R^2 \approx 0.88$–0.94) proved robust and transferable when applied to Series A. Under equivalent operating conditions, the SSF-coated configuration achieved up to 12–19% higher cooling potential than the uncoated one. Although nocturnal emissivity is similar for both materials, the PDRC coating extends effective cooling by roughly 2–4 h per day, thereby increasing the mean daily heat removal by up to 0.4 kWh/day during the experimental series studied in this work. This supports the integration of high-reflectance, high-emissivity PRC materials with hydronic radiant systems as a promising strategy for resilient, low-energy cooling in hot climates.

5. Conclusions

This experimental study shows that the Radiant-Capacity Cooling System (RCCS) can effectively reduce indoor temperatures and maintain thermal comfort for most of the testing period under hot-summer conditions through passive radiative cooling. The main findings are:

- Radiator surface performance: bare polypropylene and SSF-coated radiators reach similar nocturnal stagnation temperatures, but the PRC (SSF) coating provides clearly superior daytime sub-ambient performance and extends the effective cooling period.
- Cooling potential: the average cooling potential of the sky radiators ranged from 43.4 to 74.3 W/m^2, governed primarily by the inlet water–radiator surface temperature difference. Highest CPSR values occurred during clear nights with low minimum ambient temperatures.
- System energy performance: the RCCS removed between 2.8 and 3.2 kWh/day (432 and 494 Wh/m2•day) through the RCMs. The SSF-coated configuration (Series B) achieved ~14% higher average ERCM than the uncoated configuration (Series A), confirming the added value of advanced radiative materials.
- Influence of Flow Rate and TES Volume: lower water flow rates enhanced the heat exchange efficiency, while increasing TES volume diluted instantaneous cooling capacity but improved system stability.
- Indoor thermal conditions: mean indoor temperatures in the experimental cell were reduced by up to 7 K relative to the control cell, and daily maxima by up to 12 K relative to outdoors. These reductions substantially mitigate heat stress and demonstrate the strong potential of the RCCS as a passive/low-energy cooling strategy.
- Thermal comfort: adaptive comfort analysis showed 100% compliance in most series, even with outdoor maxima above 41 °C, indicating that the system can maintain operative temperatures within the adaptive comfort range without conventional mechanical cooling; the PMV results show that the RCCS consistently maintains indoor conditions close to thermal neutrality, with episodes of overcooling arising from the fixed operating schedule rather than from system limitations. The frequent slightly-cool values demonstrate that the system can exceed cooling demand under the tested conditions. Implementing the intended automatic control logic would align cooling output with comfort needs and stabilize PMV within the neutral range.
- Predictive models: multiple linear regression models ($R^2 > 0.88$) accurately predicted ΔTwSR and confirmed the improved performance of SSF-coated radiators, including longer effective cooling durations and higher CPSR under comparable operating conditions.

Overall, the RCCS demonstrates a reliable and energy-efficient approach to passive cooling based on sky radiative heat rejection and thermal storage integration. Its ability to maintain thermal comfort without mechanical cooling makes it a promising solution for low-energy building design, particularly in hot, dry climates.

System performance could be further improved by installing sky radiators on the roof, minimizing pipe lengths, and implementing a smart control system for dynamic management of the water circuits. Such measures would enable better use of night-time cooling to cover daytime peaks, shifting from fixed operating schedules to demand-driven operation.

Future work will address long-term durability of components, optimization and ageing of PRC coatings, and integration of the RCCS with hybrid HVAC systems for continuous, climate-adaptive operation.

"Full-scale experimental assessment of a radiant-capacitive cooling system driven by nocturnal and diurnal radiative cooling"

Glossary of terms

Abbreviations
CC control cell
CI comfort index: percentage of hours under ULACR
CP_{SR} cooling potential of the sky radiators (W/m^2)
EC experimental cell
E_{RCM} thermal energy removed in the RCMs (Wh/day, Wh/m^2.day)
ES-A experimental series without PRC material
ES-B experimental Series with PRC material
NZEB near-Zero Energy Buildings
PDRC Passive daytime radiative cooling
PRC passive radiative cooling
RCCS radiant-capacitive cooling system
RCHCS radiant-capacitive heating and cooling system
RCM radiant-capacitive module
SR sky radiator
TABs thermally activated building elements
TES thermal energy storage
ULACR upper limit of the adaptive comfort range
Nomenclature
A area (m^2)
Cp specific heat capacity (J/kgK)
DTavg mean temperature depression of Tec relative to Tamb (K)
$DT_{CC\text{-}EC}$ mean temperature depression of Tec relative to Tcc (K)
DTmax temperature depression of the maximum Tec relative to Tamb (K)
DTr reference temperature depression relative to Tamb (K)
DTsky temperature depression of Tsky relative to Tamb (K)
ΔTw_{RCM} temperature drop of water in the RCMs (K)
ΔTw_{SR} temperature drop of water in the SRs (K) d globe diameter (m) e thickness (m)
$\dot{m}$ mass flow rate of water (kg/s)
R thermal resistance (m^2K/W)
Tamb ambient or outdoor temperature (°C)
Tcc control cell indoor temperature (°C)
Tec experimental cell indoor temperature (°C)
Tg.ec globe temperature in experimental cell
Tmed 10 days prevailing mean outdoor temperature
Tmr mean radiant temperature (°C)
Tn neutral temperature (°C)
Top operative temperature (°C)
Tr2 surface temperature of polypropylene sample (°C)
Tr3 surface temperature of the polypropylene sample coated with SpaceCool Silver Film (°C)
Tsky sky temperature (K)
Tw1-9 water temperature (°C) (see Table 3 for description)
U thermal transmittance (W/m^2K)
Symbols
σ Stefan-Boltzmann constant (5.67 10^{-8} W/m^2K^4)
ε thermal emissivity
ρ thermal reflectivity
εsky emissivity
λ thermal conductivity (W/m•K)

CRediT authorship contribution statement

Eduardo González-Cruz: Conceptualization, Data curation, Formal analysis, Investigation, Methodology, Validation, Visualization, Writing – original draft, Writing – review & editing. **Gloria Pérez:** Funding acquisition, Project administration, Resources, Validation, Writing – review & editing. **Borja Frutos:** Resources, Validation, Writing – review & editing. **Carmen Alonso:** Resources, Validation, Writing – review & editing. **Fernando Martin-Consuegra:** Resources, Validation, Writing – review & editing. **Álvaro Gutierrez:** Data curation, Software. **Eduardo Krüger:** Validation, Writing – review & editing. **Lorenzo Pattelli:** Funding acquisition, Project administration, Validation, Writing – review & editing.

Declaration of competing interest

The authors declare that they have no known competing financial interests or personal relationships that could have appeared to influence the work reported in this paper.

Acknowledgements

The project (21GRD03 PaRaMetriC – Metrological framework for passive radiative cooling technologies) has received funding from the European Partnership on Metrology, co-financed from the European Union's Horizon Europe Research and Innovation Program and by the Participating States.

Supplementary materials

Supplementary material associated with this article can be found, in the online version, at doi:10.1016/j.buildenv.2026.115136.

Appendix A. Supplementary Material

Supplementary Material for this article can be found as an attached document.

Data availability

The complete experimental and atmospheric dataset collected during the analyzed series is openly available in the DIGITAL.CSIC repository at https://doi.org/10.20350/digitalCSIC/18205

References

[1] IEA, The Future of Cooling: Opportunities for Energy-Efficient Air Conditioning. Int. Energy Agency, Paris. https://www.iea.org/reports/the-future-of-cooling, Licence: CC BY 4.0 (2018).
[2] IEA, Space Cooling, IEA, Paris, 2023. https://www.iea.org/reports/space-cooling-2. Licence: CC BY 4.0.
[3] K. Joshi, A. Khan, P. Anand, J. Sen, Understanding the synergy between heat waves and the built environment: a three-decade systematic review informing policies for mitigating urban heat island in cities, Sustain. Earth Rev. 7 (1) (2024) 25, https://doi.org/10.1186/s42055-024-00094-7.
[4] C.G. Granqvist, A. Hjortsberg, Radiative cooling to low temperatures: general considerations and application to selectively emitting SiO films, J. Appl. Phys. 52 (1981) 4205–4220, https://doi.org/10.1063/1.329270.
[5] M.N. Bahadori, Passive cooling systems in Iranian architecture, Sci. Am. 238 (2) (1978) 144–154.
[6] F. Trombe, Nouvelles experiences sur le refroidissement de corps noirs rayonnant sur l'espace, Comptes Rendus 256 (1963) 2013–2015.
[7] H.R. Hay, J.I. Yellott, International aspects of air conditioning with movable insulation, Sol. Energy 12 (4) (1969) 427–438, https://doi.org/10.1016/0038-092X(69)90065-6.
[8] H.R. Hay, How to stop cooling loads before they start, in: Proceedings: solar cooling for buildings, Los Angeles, CA 6-–8, 1974, p. 612.
[9] B. Givoni, Passive Low Energy Cooling of Buildings, John Wiley & Sons, 1994.
[10] M. Santamouris, D. Asimakopoulos (Eds.), Passive Cooling of Buildings, Earthscan, 1996.
[11] E.M. González-Cruz, E.L. Krüger, Experimental study on a low energy radiant-capacitive heating and cooling system, Energy Build. 255 (2022) 111674, https://doi.org/10.1016/j.enbuild.2021.111674.
[12] S. Catalanotti, V. Cuomo, G. Piro, D. Ruggi, V. Silvestrini, G. Troise, The radiative cooling of selective surfaces, Sol. Energy 17 (2) (1975) 83–89, https://doi.org/10.1016/0038-092X(75)90062-6.
[13] L. Jia, L. Lu, A vertical fin-intensified radiative sky cool method for heat rejection: insights from the comparative study of cooling technologies, Appl. Therm. Eng. 290 (2026) 130109, https://doi.org/10.1016/j.applthermaleng.2026.130109.

[14] L. Jia, L. Lu, J. Chen, Q. Gong, Model development of deep space-source heat pump system and its feasibility analysis, J. Clean. Prod. 430 (2023) 139556, https://doi.org/10.1016/j.jclepro.2023.139556.

[15] A.P. Raman, M. Abou Anoma, L. Zhu, E. Rephaeli, S. Fan, Passive radiative cooling below ambient air temperature under direct sunlight, Nature 515 (7528) (2014) 540–544, https://doi.org/10.1038/nature13883.

[16] B. Zhao, M. Hu, X. Ao, N. Chen, G. Pei, Radiative cooling: a review of fundamentals, materials, applications, and prospects, Appl. Energy 236 (2019) 489–513, https://doi.org/10.1016/j.apenergy.2018.12.018.

[17] D. Zhao, A. Aili, Y. Zhai, S. Xu, G. Tan, X. Yin, R. Yang;, Radiative sky cooling: fundamental principles, materials, and applications, Appl. Phys. Rev. 6 (2) (2019) 021306, https://doi.org/10.1063/1.5087281.

[18] Q. Zhang, S. Wang, X. Wang, Y. Jiang, J. Li, W. Xu, J. Zhu, Recent progress in daytime radiative cooling: advanced material designs and applications, Small Methods 6 (4) (2022) 2101379, https://doi.org/10.1002/smtd.202101379.

[19] W. Gao, Y. Chen, Emerging materials and strategies for passive daytime radiative cooling, Small 19 (18) (2023) 2206145, https://doi.org/10.1002/smll.202206145.

[20] R. Liu, S. Wang, Z. Zhou, K. Zhang, G. Wang, C. Chen, Y. Long, Materials in radiative cooling technologies, Adv. Mater. 37 (2) (2025) 2401577, https://doi.org/10.1002/adma.202401577.

[21] Y. Dong, Z. Yang, Z. Cheng, F. Hua, C. Wang, Y. Yan, F. Wang, Application-driven daytime radiative cooling: from optical properties to functional customization, ACS Appl. Mater. Interfaces 18 (2026) 6300–6328, https://doi.org/10.1021/acsami.5c20790.

[22] B. Tian, X. Fan, Z. Yang, J. Ge, X. Li, P. Huang, F. Wang, Performance effects and analysis of passive daytime radiative cooling coatings under environmental aging conditions, Int. J. Heat. Mass Transf. 263 (2026) 128700, https://doi.org/10.1016/j.ijheatmasstransfer.2026.128700.

[23] U. Berardi, S. Soudian, Outdoor test facilities for the experimental performance evaluation of construction materials and systems: the BeTOP case, Case Stud. Constr. Mater. 18 (2023) e01920, https://doi.org/10.1016/j.cscm.2023.e01920.

[24] J. Le Dréau, P. Heiselberg, R.L Jensen, A full-scale experimental set-up for assessing the energy performance of radiant wall and active chilled beam for cooling buildings, Build. Simul. 8 (2015) 39–50, https://doi.org/10.1007/s12273-014-0190-7.

[25] M. Andrés-Chicote, A. Tejero-González, E. Velasco-Gómez, F.J. Rey-Martínez, Experimental study on the cooling capacity of a radiant cooled ceiling system, Energy Build. 54 (2012) 207–214, https://doi.org/10.1016/j.enbuild.2012.07.043.

[26] S. Wang, L. Yang, Y. Liu, J. Pang, L. Yang, M. Dou, Full-scale experimental study of the surface cooling effect of prefabricated buildings utilizing passive radiative cooling under real operating conditions, Energy 328 (2025) 136472, https://doi.org/10.1016/j.energy.2025.136472.

[27] E.M. González-Cruz, E. Krüger, F. Carraro, G.M. De Bem, A.A.M. de Abreu, D. Trento, Implementação de um sistema de aquecimento e resfriamento radiante-capacitivo (RC-HCS) em uma câmara climática, Encontro Nac. Tecnol. Amb. Constr. 19 (2022) 1–16, https://doi.org/10.46421/entac.v19i1.2026.

[28] B. Arranz, I. Oteiza, E.M. Delgado, Á. Gutiérrez, Construcción y monitorización del Laboratorio REVen para el estudio del impacto de las ventanas integrando eficiencia energética y calidad ambiental interior, Inf. Constr. 72 (557) (2020) e324, https://doi.org/10.3989/ic.67523.

[29] M.G. Delgado, J.S. Ramos, S.Á. Dominguez, Using the sky as heat sink: climatic applicability of night-sky based natural cooling techniques in Europe, Energy Convers. Manag. 225 (2020) 113424, https://doi.org/10.1016/j.enconman.2020.113424.

[30] R. Vilà, M. Medrano, A. Castell, Mapping nighttime and all-day radiative cooling potential in Europe and the influence of solar reflectivity, Atmosphere 12 (2021) 1119, https://doi.org/10.3390/atmos12091119.

[31] D. Forte, E. González-Cruz, L. Pattelli, C. Belotti, G. Pérez, P. Asinari, M. Fasano, Sky cooling-driven radiant-capacitive hydronic system for all-day building cooling, Appl. Energy 406 (2026) 127260, https://doi.org/10.1016/j.apenergy.2025.127260.

[32] E.M. González-Cruz, S.I. González-García, Estudio experimental sobre el comportamiento térmico de un nuevo tipo de techo-estanque para el enfriamiento pasivo en clima húmedo, Amb. Constr. 13 (2013) 149–171.

[33] B. Lehmann, V. Dorer, M. Koschenz, Application range of thermally activated building systems tabs, Energy Build 39 (5) (2007) 593–598, https://doi.org/10.1016/j.enbuild.2006.09.009.

[34] J. Romaní, A. De Gracia, L.F. Cabeza, Simulation and control of thermally activated building systems (TABS), Energy Build. 127 (2016) 22–42, https://doi.org/10.1016/j.enbuild.2016.05.057.

[35] Y. Li, C. Mclauchlan, X. Gong, Z. Ma, Experimental and modeling investigation of thermally activated building systems integrated with ground source heat pump systems, Energy Build. 328 (2025) 115210, https://doi.org/10.1016/j.enbuild.2024.115210.

[36] SOLAPOOL Homepage, https://www.saclima.com/categoria-producto/solapool/captadores/, (Accessed 2025/09/29).

[37] SpaceCool Homepage, https://spacecool.jp/en/product/film/, (Accessed 2025/09/29).

[38] A. Adibekyan, J. Schumacher, L. Pattelli, J. Manara, S. Meriç, Ö Bazkir, C. Cucchi, C. Sprengard, G. Pérez, J. Campos, et al., Emissivity and reflectivity measurements for passive radiative cooling technologies, Int. J. Thermophys. 46 (5) (2025) 1–16, https://doi.org/10.1007/s10765-025-03532-6.

[39] F.M. Mims III, L.H. Chambers, D.R Brooks, Measuring total column water vapor by pointing an infrared thermometer at the sky, Bull. Am. Meteorol. Soc. 92 (10) (2011) 1311–1320, https://doi.org/10.1175/2011BAMS3215.1.

[40] Y. Etzion, Erell, Low-cost long-wave radiators for passive cooling of buildings, Arch. Sci. Rev. 42 (2) (1999) 79–85.

[41] ANSI/ASHRAE Standard 55-2020, Thermal Environmental Conditions for Human Occupancy, ASHRAE, Atlanta, 2020.

[42] ISO 7726, Ergonomics of the Thermal Environment - Instruments for Measuring Physical Quantities, International Organization for Standardization, Geneva, Switzerland, 1998. Current as of 2021.

[43] F. Tartarini, S. Schiavon, T. Cheung, T. Hoyt, CBE thermal comfort tool : online tool for thermal comfort calculations and visualizations, SoftwareX 12 (2020) 100563, https://doi.org/10.1016/j.softx.2020.100563.

[44] T.Z Keith, Multiple Regression and Beyond, Routledge, Taylor & Francis Group, NY, 2019, https://doi.org/10.4324/9781315162348.

[45] A. Adibekyan, C. Alonso, M. Arduini-Schuster, M.N. Assimakopoulos, O. Bazkir, C. Belotti, Campos-Acosta, Report on the validated reference techniques used for emittance and reflectance measurements of PRC materials in the spectral range 0.25 μm –50 μm, with a target uncertainty below 3 % for emissivity and absorptivity, Zenodo (2025), https://doi.org/10.5281/zenodo.17684600.